Coherent coupling between radio frequency, optical, and acoustic waves in piezo-optomechanical circuits

Krishna C. Balram,[1,2,*] Marcelo I. Davanço,[1] Jin Dong Song,[3] and Kartik Srinivasan[1,†]

[1]*Center for Nanoscale Science and Technology,*

National Institute of Standards and Technology, Gaithersburg, MD 20899, USA

[2]*Maryland NanoCenter, University of Maryland, College Park, MD 20742, USA*

[3]*Center for Opto-Electronic Materials and Devices Research,*

Korea Institute of Science and Technology, Seoul 136-791, South Korea

(Dated: March 30, 2016)

Abstract

Optomechanical cavities have been studied for applications ranging from sensing to quantum information science. Here, we develop a platform for nanoscale cavity optomechanical circuits in which optomechanical cavities supporting co-localized 1550 nm photons and 2.4 GHz phonons are combined with photonic and phononic waveguides. Working in GaAs facilitates manipulation of the localized mechanical mode either with a radio frequency (RF) field through the piezo-electric effect, which produces acoustic waves that are routed and coupled to the optomechanical cavity by phononic crystal waveguides, or optically through the strong photoelastic effect. Along with mechanical state preparation and sensitive readout, we use this to demonstrate an acoustic wave interference effect, similar to atomic coherent population trapping, in which RF-driven coherent mechanical motion is cancelled by optically-driven motion. Manipulating cavity optomechanical systems with equal facility through both photonic and phononic channels enables new architectures for signal transduction between the optical, electrical, and mechanical domains.

1

Introduction

The interaction of optical and mechanical degrees of freedom in chip-based nanoscale systems has been studied in many contexts, ranging from optomechanical cavities[1–4] in which localized optical and mechanical modes are coupled by radiation pressure, to waveguiding geometries in which propagating photons and phonons interact, as in stimulated Brillouin scattering[5–7] (the latter has also been studied in travelling-wave microresonators[8–10]). Recently there has been interest in combining the exquisite motion sensitivity of cavity optomechanical systems[11] with the radio frequency (RF) signal processing functionality of electromechanical systems to enable wavelength conversion between microwave and optical domains[12], electrostatically-actuated optomechanical cavities for sensing and feedback cooling[13,14], and piezo-optomechanical cavities[15,16] in which mechanical motion is driven by RF fields, with sensitive readout and coherent interference effects observable in the optical domain.

Here, we develop a platform in which a nanoscale optomechanical cavity is embedded in a larger system that enables access through both photonic and RF-driven phononic channels. Working in GaAs allows us to combine its photoelastic effect, which strongly couples localized optical and mechanical modes[17,18], with its piezoelectric behaviour, which enables the RF-driven generation of acoustic waves through an interdigitated transducer[19]. The generated acoustic waves are fed into phononic crystal waveguides that route and preferentially couple acoustic energy to the 2.4 GHz breathing mode of nanobeam optomechanical crystal cavities[18,20,21]. We use this combination of RF-driven acoustic waveguides and strong optomechanical coupling ($g_0/2\pi \approx 1.1$ MHz is more than one order of magnitude larger than that achieved in recent piezo-optomechanical cavities[15,16]) to demonstrate a number of effects. Phase-sensitive optical measurements confirm the ability to initialize the mechanical resonator with arbitrary amplitude and phase, and with an average coherent intracavity phonon population much less than one. We also observe a novel acoustic wave interference effect, similar to atomic coherent population trapping, in which RF-driven coherent motion of the mechanical resonator is cancelled by optically-induced motion, and vice versa. This demonstration of an optomechanical circuits platform which combines controlled excitation, routing, coupling, and detection of both propagating and localized photons and phonons will enable new applications of integrated electro-optomechanical systems in signal transduction and sensing.

Results

Figure 1(a) shows an overview of our platform[22]. The system uses an inter-digitated transducer

(IDT) to convert an applied RF voltage to a propagating surface acoustic wave via the piezoelectric effect. This wave is routed using a phononic crystal waveguide and is butt-coupled to a nanobeam optomechanical crystal cavity (Fig. 1(c)-(d)). The optical interface to the cavity is via a fibre taper waveguide, which injects and extracts light from the device. Finally, a second IDT can electrically detect acoustic waves out-coupled from the cavity, or act as a second source of surface acoustic waves that couple to the cavity via a second phononic crystal waveguide.

Coupling Propagating and Localized Phononic Modes

Figure 1(b) shows the optomechanical crystal cavity design, which consists of an array of elliptical air holes in a suspended nanobeam[18]. The quadratic grade of the lattice constant and major and minor axis diameters of the elliptical holes co-localizes 1550 nm photons and 2.4 GHz phonons to a micrometre length scale. The optomechanical coupling rate $g_0/2\pi$, which is the optical cavity frequency shift due to zero-point motion, is $\approx$ 1.1 MHz and is dominated by the photoelastic effect. This is amongst the highest reported for an optomechanical cavity, and enables strong dynamic back-action so that the optical field can coherently manipulate the localized mechanical breathing mode. For RF-mediated coherent control of the mechanical mode, we need to convert the RF voltage into an acoustic wave and route and couple the acoustic wave to the cavity. We begin by considering acoustic wave generation.

Surface acoustic waves (SAWs) have long been used in signal processing and communication[23,24]. Piezoelectric materials are used most extensively because of the ease of SAW excitation using IDTs, which are interleaved metal fingers biased with opposite polarity[22]. To take into account the multilayer metal electrode and underlying epitaxial layer structure (GaAs on $Al_{0.7}Ga_{0.3}As$), the IDT resonance frequency is determined from finite element method (FEM) simulations. Figure 2(a) shows the simulated SAW cross-section.

To route acoustic energy to the optomechanical cavity, we use phononic crystal waveguides. The phononic crystal design is adapted from the periodic cross-structure[25], which supports a complete bandgap[22]. The waveguide is a line defect geometry created by removing one row of crosses, resulting in a structure that supports laterally-confined, propagating acoustic modes. Figure 2(a) shows an FEM simulation of an acoustic wave excited by an IDT and propagating through the waveguide. The phononic crystal confines mechanical energy to the line defect region, with little displacement beyond a couple of periods transverse to the propagation direction.

We use FEM simulations to understand coupling between the localized and propagating mechanical modes. Figure 2(b) shows a simulation in which the waveguide mode at 2.25 GHz is

3

launched into the nanobeam cavity, with excitation of the resonant mechanical breathing mode clearly observed. This coupling can be understood quantitatively from the cavity's acoustic reflection spectrum[22]. The finite intrinsic Q_m of the cavity in fabricated devices is modeled by a small imaginary component in the Young's modulus, with the magnitude adjusted for different Q_m. The reflection spectra (Fig. 2(b) inset) show the expected Lorentzian dip as the waveguide mode frequency sweeps over the cavity, with the depth determined by the coupling rate relative to the cavity intrinsic loss rate. For $Q_m = 1500$ (typical for our devices), the reflection contrast is limited to ≈ 15 %, while an improved intrinsic Q_m of 2.5×10^4 would enable critical coupling. Alternately, the transition between waveguide and cavity, or the waveguide geometry itself, can be tailored to modify the coupling rate. In contrast to recent work in which surface acoustic waves non-resonantly excited microring[26] and photonic crystal cavities[27], these simulations indicate that we can resonantly excite the localized mechanical mode of our nanobeam optomechanical crystal cavity. This is important for the experiments we describe going forward, given the large optomechanical coupling strength for this mode and its direct impact on high-sensitivity readout and manipulation of mechanical motion.

Experimentally, the IDT frequency response is measured by an electrical S_{11} (reflection) measurement. The top panel of Fig. 2(d) shows the S_{11} spectra for IDTs with electrode finger pitches of 1.05 μm and 1.1 μm. Optimal loading of the localized mechanical mode by the RF drive occurs when the mode frequency lies within the IDT bandwidth. The bottom panel of Fig. 2(d) shows the scaling of the IDT resonance frequency with finger pitch in simulation and experiment, along with the desired region of operation shaded in gray (corresponding to the nanobeam breathing mode frequency range). To ensure that some fabricated devices show the required spectral overlap, each IDT addresses an array of optomechanical cavities (Fig. 1(a)), and the nanobeam width is varied across the array, thereby tuning the localized mechanical mode frequency with respect to a fixed IDT frequency[22].

While IDTs are a convenient means to generate propagating acoustic waves, the relatively small piezoelectric transduction coefficient of GaAs[23] limits the conversion efficiency back to the RF domain for electrical readout. Thus, for sensitive detection of the nanobeam cavity's motion when driven by the propagating acoustic wave, we use the strong photoelastic coupling for optical readout. The setup is shown in Fig. 2(c), where light is injected into the optomechanical cavity using an optical fibre taper waveguide, and a vector network analyzer (VNA) drives the IDT with an RF voltage and coherently detects the photocurrent signal transmitted past the optomechanical

cavity, yielding a piezo-optic S_{21} measurement. The laser wavelength is positioned on the shoulder of the optical mode ($Q_{opt} = 36600 \pm 400$, fit uncertainty 95 % confidence intervals)[22], so that the phase fluctuations induced by motion are transduced into an intensity-modulated optical signal.

The bottom panel of Fig. 2(e) shows the measured piezo-optic S_{21} in two instances. First (red curve), a phononic crystal waveguide butt-coupled to the optomechanical cavity is adjacent to the RF-driven IDT (IDT 1, Fig. 2(c)), and a pronounced peak $\approx$ 20 dB above the background is observed at the nanobeam cavity's mechanical mode frequency, as confirmed by direct detection of its thermal noise spectrum (top panel of Fig. 2(e)). In the second case (blue curve), an unperturbed phononic shield spans the region between the cavity and RF-driven IDT (IDT 2, Fig. 2(c)). Here, the piezo-optic S_{21} is suppressed by more than 30 dB relative to the first case, indicating that the phononic shield effectively blocks the transmission of acoustic energy from the IDT to the cavity.

Coherent Mechanical State Preparation and Readout

Next, we phase coherently load mechanical states into our optomechanical cavity via the phononic waveguide, and show that the optical readout is sensitive enough to distinguish a fraction of a coherent phonon from the thermal phonon population ($N_{avg} \approx 2600$) and measurement noise. Figure 3(a) shows the setup (see Methods), where in comparison to Fig. 2(c), we now additionally provide RF phase control, calibration of the optomechanical coupling rate, and measurement of the total RF power spectral density (PSD), consisting of the incoherent thermal motion of the mechanical resonator, its driven coherent motion due to surface acoustic wave excitation, and the phase modulator calibration tone.

Figure 3(b) displays the piezo-optic S_{21} measurement of coherently-driven motion similar to Fig. 2(e), but now for an optomechanical cavity connected to input/output phononic waveguides (Fig. 3(a)). The results are similar, with the piezo-optic S_{21} showing a peak corresponding to the cavity's mechanical resonance frequency and which lies within the IDT's resonance bandwidth. The importance of this overlap is shown in Fig. 3(e)-(f), which contrasts the RF power applied to the IDT to achieve a certain coherent intracavity phonon population when the localized nanobeam mechanical mode is on-resonance with the IDT (Fig. 3(c)) to when it is off-resonance with the IDT (Fig. 3(d)). Two nanobeam cavities from the same array were chosen, so that the IDT characteristics were fixed as the nanobeam mechanical frequency changed. Off resonance, nearly 20 dB greater RF input power is needed to achieve the same strength of the coherent tone in the photodetected signal, reflecting the resonant nature of the IDT.

We quantify the average coherent intracavity phonon number $N_{\text{ph}}^{\text{coh}}$ by comparing the strength

of the coherent tone with that due to the integrated thermally-driven motion $S_{\text{th}}(\Omega_m)$. That is:

$$N_{\text{ph}}^{\text{coh}} = \frac{k_{\text{B}}T}{\hbar\Omega_m} \frac{S_{\text{coh}}(\Omega_{\text{coh}})}{S_{\text{th}}(\Omega_m)} \tag{1}$$

where k_{B} is Boltzmann's constant, T is temperature (298 K $\pm$ 5 K), Ω_m is the mechanical mode frequency, $S_{\text{coh}}(\Omega_{\text{coh}})$ is the power in the coherent tone, and $S_{\text{th}}(\Omega_m)$ is the integrated power in the thermal noise peak. $N_{\text{ph}}^{\text{coh}} = 43 \pm 1.5$ for Fig. 3(e) and $N_{\text{ph}}^{\text{coh}} = 50 \pm 1.8$ for Fig. 3(f), quantifying the increased RF drive needed to achieve a given $N_{\text{ph}}^{\text{coh}}$ when the nanobeam mechanical resonance and IDT are spectrally misaligned. Finally, we use the phase modulator to measure $g_0/2\pi = 1.1$ MHz $\pm$ 60 kHz, corresponding well with simulations[18], and with a one standard deviation uncertainty set by the uncertainty in the phase modulator V_{π}[22].

We can also consider the device in Fig. 3(c) as a resonant acousto-optic phase modulator (an exact comparison in the sideband-resolved regime), and determine its half-wave voltage $V_{\pi} \approx 652$ mV[22]. This can be reduced to $V_{\pi} < 100$ mV by optimizing the coupling to the optomechanical cavity and minimizing both RF and acoustic reflections and scattering at interfaces. Recently, Li and colleagues have demonstrated up to 12 GHz on-chip acousto-optic modulators in which surface acoustic waves modulate the response of a photonic crystal cavity[27]. In contrast to this work and earlier papers[19,26], here the propagating acoustic waves are laterally confined and resonantly couple to localized mechanical modes. The localized mechanical resonance enhances the modulation efficiency (by $\sim \sqrt{Q_m}$) without creating a significant bandwidth restriction beyond that already imposed by the IDT[22]. Moreover, such localized mechanical modes are typically more strongly coupled to localized optical modes.

For coherent control of the resonator, we need to transfer both the RF amplitude and phase onto the cavity displacement. Figure 3(g) plots the in-phase and quadrature components of the photodetected signal on-resonance for different phases applied to the IDT. Th e data is displayed as a function of average coherent mechanical displacement, where the calibration described in the previous paragraph is used to determine $N_{\text{ph}}^{\text{coh}}$, which in turn is converted to a displacement by:

$$N_{\text{ph}}^{\text{coh}} = \frac{1}{2}\left(\frac{\alpha_{\text{cav}}}{x_{\text{zpf}}}\right)^2 \tag{2}$$

where α_{cav} is the magnitude of the coherent cavity displacement and $x_{\text{zpf}} = \sqrt{\frac{\hbar}{2m_{\text{eff}}\Omega_m}}$ is the zero-point motional amplitude ($m_{\text{eff}} \approx 0.5$ pg is the simulated effective mass). The data shows that a

variation in amplitude and phase of the RF signal is mapped onto the localized mechanical mode, and it can be initialized at an arbitrary location in phase space. These measurements confirm that coherence is preserved through the process of converting an RF voltage to an acoustic wave that propagates through a phononic crystal waveguide and couples to an optomechanical crystal cavity. By injecting acoustic waves with similar amplitudes and varying phase difference through two phononic waveguides that excite the same optomechanical cavity, we can observe constructive and destructive interference effects occurring within the mechanical resonator[22].

The combination of coherent detection and the large optomechanical coupling strength enables measurement of a weak coherent intracavity phonon population on top of the ≈ 2600 thermal phonons in the cavity. In Fig. 3(h), we reduce the RF amplitude and measure the mechanical motion on-resonance, displayed as a polar plot in terms of the phonon number and phase angle. Figure 3(i) shows the data plotted against motional amplitude for the three smallest RF drives, where for each the data has been histogrammed into 15 equally-spaced bins. $N_{\text{ph}}^{\text{coh}} \approx 1.1$ is well-separated from the measurement noise floor (RF set to zero), and $N_{\text{ph}}^{\text{coh}}$ as low as ≈ 0.05 is resolvable. We also display the PSD for $N_{\text{ph}}^{\text{coh}} < 1$ (Fig. 3(h) inset). The minimum detectable $N_{\text{ph}}^{\text{coh}} \approx 0.05$ is approximately $20\times$ smaller than in Ref. 15, and is primarily due to the significantly larger optomechanical coupling rate of 1.1 MHz (compared to 30 kHz in Ref. 15).

Coherent Interactions between RF, Optics, and Mechanics

Thus far, we have shown that phononic crystal waveguides sourced by IDTs can effectively couple acoustic energy to the localized mechanical mode of a nanobeam optomechanical cavity. In these experiments, large g_0 enables sensitive optical readout of the mechanical motion, but was not used to manipulate the mechanical resonator. We next consider experiments in which the mechanical resonator is simultaneously excited using both RF signals and optical fields. This highlights a key feature of the GaAs optomechanical circuit platform, which is that the motion of the mechanical resonator can be manipulated with similar facility along either the optical or RF channel.

Figure 4(a) shows a schematic indicating the couplings and decay channels of the different components in our system. If we ignore the states that depict the phononic waveguide, its feeding from an IDT, and coupling to the phononic cavity, we recover the characteristic Λ-system configuration in which optomechanically induced transparency (OMIT)[28–30] has been observed in many systems. Adding the new channel provides us with another knob to coherently control and probe the system properties and observe new phenomena. The interference effect we describe

in this section occurs in the phononic cavity, which can be driven optically via the beating of probe and control lasers that are detuned from each other by the mechanical mode frequency (as in OMIT), or acoustically through the phononic waveguide. These two pathways can be tuned to have equal amplitudes and opposite phases, resulting in a cancellation of the coherent motion of the mechanical resonator. This effect is qualitatively similar to coherent population trapping in atomic systems[31,32], and has not been previously discussed or observed in recent studies of piezo-optomechanical systems[15,16,26,27].

Starting with the coupled equations of cavity optomechanics, one can derive an expression for the steady-state cavity displacement amplitude β_{d+}[22]:

$$\beta_{d+} = \frac{-ig_0(\alpha_0\alpha_{d-}^*) - \sqrt{\frac{\gamma_e}{2}}\beta_{in,0}e^{i\psi}}{i(\Omega_m - \Omega_d) + \frac{\gamma_i}{2}} \tag{3}$$

The first term in the numerator corresponds to the optical drive due to beating of the intracavity control (α_0) and probe (α_{d-}) beams, and the second term corresponds to the acoustic drive ($\beta_{in,0}e^{i\psi}$) through the phononic waveguide coupling to the cavity (coupling rate γ_e and intrinsic decay rate γ_i). Appropriate choice of the amplitude ($\beta_{in,0}$) and phase (ψ) of the acoustic drive produces the condition for cancellation of the mechanical mode ($\beta_{d+} = 0$):

$$\sqrt{\frac{\gamma_e}{2}}\beta_{in,0}e^{i\psi} = \frac{-i\sqrt{\frac{\kappa_e}{2}}g_0\alpha_0\alpha_{in,-}^*}{-i(\Delta + \Omega_d) + \frac{\kappa_i}{2}} \tag{4}$$

wherein $\alpha_{in,-}$ represents the input probe signal, Δ the laser-cavity detuning, Ω_d the probe beam detuning from the control beam frequency, κ_e the optical cavity coupling rate, and κ_i the intrinsic optical cavity decay rate.

When this condition is satisfied, the coherent cavity displacement tends to zero and the cavity transmission is flat over the mechanical resonator bandwidth (the system acts as a pure optical cavity for the probe). Only the coherently driven component of the cavity displacement becomes zero, as the cavity is still driven by incoherent thermal motion and has a finite PSD. We also distinguish this effect from other phenomena observed in cavity optomechanics. Both OMIT and electromechanically-induced optical transparency[15,16] are effects in which probe photons optically interfere with light scattered off a driven mechanical resonator, and the mechanical resonator has a finite coherent displacement amplitude at all times. The effect we observe is similar to the optomechanical dark mode[33,34] established in coherent wavelength conversion[34–36], although in that work coherent mechanical motion is suppressed purely though optomechanical coupling.

Figure 4(b) shows the experimental setup used to probe the coherent interaction between RF, optics, and mechanics, where the RF signals driving the IDT and electro-optic phase modulator are coherent but can differ in amplitude and overall phase (see Methods). Figure 4(c) shows a series of piezo-optical S_{21} measurements performed as the VNA output frequency is swept across the mechanical resonance and the RF power into the IDT is increased, along with calculations of the expected S_{21} spectrum and corresponding mechanical resonator displacement amplitude[22]. The topmost black curves are for the IDT channel turned off, and correspond to the pure OMIT case. We then increase the RF power while keeping the phase fixed to satisfy the condition for acoustic wave interference. As the RF power is increased, the OMIT peak is reduced and at a particular RF power (cyan curves in Fig. 4(d)), the transmission spectrum reaches zero on-resonance and is approximately (perfectly) spectrally flat in experiment (theory). This corresponds to complete suppression of the coherent cavity displacement and removal of the transparency window that was initially induced by the optomechanical interaction. The inability to achieve perfect spectral flatness in experiment is attributed to the actuation of other mechanical modes that occurs electrically but not optically[22]. With further increase in the RF power, the cavity is primarily driven by the phononic waveguide and the cavity displacement amplitude increases correspondingly (magenta, yellow, dark gray curves). Since the phase is set for destructive interference, the probe transmission drops and the interference feature within the optical cavity spectrum re-appears (the system is now in the regime of electromechanically-induced optical transparency[15,16]). Here, the mechanical breathing mode is in the same state as in pure OMIT, except that the displacement has the opposite phase and so transparency is converted to absorption.

A more complete picture is observed by measuring the in-phase and quadrature components of the on-resonance photodetected signal (Fig. 4(d)). Starting with the pure OMIT condition (IDT turned off, Fig. 4(e), curve i), as we increase the RF drive to the IDT, for the right choice of phase the cavity displacement approaches zero (Fig. 4(e), curve ii), and the signal on-resonance is equal to its off-resonance value (Fig. 4(e), dashed circle). Further increase in the RF power moves the system into the region of induced absorption (Fig. 4(e), curve iii), while other parts of phase space are accessed by varying the phase applied to the IDT. For an arbitrary phase, the response of the system is given by an asymmetric Fano lineshape (for example, Fig. 4(e), curve iv).

Discussion

We have presented an integrated piezo-optomechanical circuit platform in which fibre-coupled GaAs optomechanical crystal cavities are interfaced with phononic waveguides and interdigi-

tated transducers. This system combines localized and interacting 1550 nm photons and 2.4 GHz phonons with excitation and readout along either the optical or mechanical channel, with the latter connected to the RF domain via IDTs. As GaAs is both piezoelectric and has a strong photoelastic effect, the mechanical resonator can be effectively manipulated by both RF and optical fields, enabling potential applications such as RF-controllable optomechanically-induced transparency for slow light and delay lines[30] and phononic routing between cavity optomechanical nodes for quantum networks[37,38]. Generation of acoustic waves with optimized IDTs[23,39] or through optical means via stimulated Brillouin scattering[5–7] and developments in chip-based phononics[40,41,41–44] can improve future circuitry to interface with the optomechanical cavities. Finally, incorporation of InAs/GaAs quantum dots[45–47], which have been used in many quantum optics applications[48] and are compatible with the device fabrication described here, would add qualitatively new functionality.

Methods

Measurement methods

Light from a 1520 nm to 1630 nm tunable laser is coupled into and out of the optomechanical cavities using an optical fibre taper waveguide with a minimum diameter of ≈ 1 μm, with the output optical signal photodetected by an avalanche photodiode (APD). For coherent excitation and detection of mechanical motion (piezo-optic S_{21}) as in Fig. 2(c), a vector network analyzer (VNA) excites a source IDT and reads out the coherent component of the photodetected signal. To initialize the mechanical resonator at an arbitrary location in phase space, an RF phase shifter is placed between the VNA output and source IDT (Fig. 3(a)). For simultaneous excitation of the mechanical resonator by both RF and optical fields, the output of the VNA is split into two paths, with one path driving an electro-optic phase modulator inserted at the output of the tunable laser, and the other path sent through an RF amplifier and phase shifter before going to the source IDT (Fig. 4(b)). This enables control of the amplitude and phase of the RF signal driving the IDT with respect to that driving the phase modulator. In these experiments (Fig. 4), the control laser power is fixed and is blue-detuned by a mechanical resonance frequency from the optical cavity resonance.

Measurement of the total photodetected signal (not just the coherent component) is obtained by sending it to a real-time RF spectrum analyzer (RSA) (Fig. 3(a)); this is used to calibrate the coherent intracavity phonon number with respect to thermal noise. Finally, a second RF signal generator is used for calibration of the optomechanical coupling rate g_0 (Fig. 3(a)), as discussed in detail in the supplementary material[22].

10

Fabrication

A detailed description of the fabrication procedure is provided in the supplementary material[22], and a brief summary is provided here. The IDTs are defined first through electron-beam lithography and metal lift-off. After electrical S_{11} measurements to determine the IDT resonance frequencies, the phononic crystal waveguides and nanobeam optomechanical crystal patterns are overlaid with a second electron-beam lithography step that uses alignment marks defined during the IDT fabrication. The patterns are then transferred to the GaAs layer using an Ar/Cl$_2$ inductively-coupled plasma reactive ion etch step. The devices are finally released using a timed wet etch.

Simulations

A detailed description of all the simulation procedures is provided in the supplementary material[22], and a brief summary is provided here. First, we use a finite element method (FEM) solver to calculate both the resonance frequency of the nanobeam cavity's localized mechanical mode and the surface acoustic wave generated by the IDT for a given pitch. In a separate simulation, this IDT-generated surface acoustic wave is launched into the phononic crystal line defect waveguide, and penetration of mechanical energy into the surrounding phononic shield was examined as a function of acoustic wave frequency. The coupling between the phononic crystal waveguide and nanobeam optomechanical cavity was calculated by defining an acoustic Poynting vector and solving for the transmitted and reflected acoustic power as a function of frequency. For the acoustic wave interference simulations, the coupled equations for intracavity optical field amplitude and mechanical displacement were solved numerically by linearizing around the steady-state values. Finally, the nanobeam optomechanical cavity's optical modes were solved using an FEM solver, and the optomechanical coupling rate to the localized mechanical breathing mode was determined from a calculation based on perturbation theory, taking into account the effect of both moving dielectric boundaries and the photoelastic effect.

---

* Electronic address: `krishna.coimbatorebalram@nist.gov`

† Electronic address: `kartik.srinivasan@nist.gov`

1 Aspelmeyer, M., Kippenberg, T.J. & Marquardt, F. Cavity optomechanics. *Rev. Mod. Phys.* **86**, 1391 (2014).

2 Metcalfe, M. Applications of cavity optomechanics. *Applied Physics Reviews* **1**, 031105 (2014).

3 Favero, I. & Karrai, K. Optomechanics of deformable optical cavities. *Nature Photon.* **3**, 201–205

(2009).

[4] Kippenberg, T.J. & Vahala, K.J. Cavity Optomechanics: Back-Action at the Mesoscale. *Science* **321**, 1172–1176 (2008).

[5] Pant, R. *et al.* On-chip stimulated brillouin scattering. *Opt. Express* **19**, 8285–8290 (2011).

[6] Shin, H. *et al.* Tailorable stimulated Brillouin scattering in nanoscale silicon waveguides. *Nature Commun.* **4** (2013).

[7] Van Laer, R., Kuyken, B., Van Thourhout, D. & Baets, R. Interaction between light and highly confined hypersound in a silicon photonic nanowire. *Nature Photon.* **9**, 199–203 (2015).

[8] Matsko, A., Savchenkov, A., Ilchenko, V., Seidel, D. & Maleki, L. Optomechanics with surface-acoustic-wave whispering-gallery modes. *Phys. Rev. Lett.* **103**, 257403 (2009).

[9] Bahl, G., Zehnpfennig, J., Tomes, M. & Carmon, T. Stimulated optomechanical excitation of surface acoustic waves in a microdevice. *Nature Commun.* **2**, 403 (2011).

[10] Li, J., Lee, H. & Vahala, K.J. Microwave synthesizer using an on-chip brillouin oscillator. *Nature Commun.* **4** (2013).

[11] Wilson, D.J. *et al.* Measurement-based control of a mechanical oscillator at its thermal decoherence rate. *Nature (London)* **524**, 325–329 (2015).

[12] Andrews, R. *et al.* Bidirectional and efficient conversion between microwave and optical light. *Nature Phys.* **10**, 321–326 (2014).

[13] Winger, M. *et al.* A chip-scale integrated cavity-electro-optomechanics platform. *Opt. Express* **19**, 24905–24921 (2011).

[14] Miao, H., Srinivasan, K. & Aksyuk, V. A microelectromechanically controlled cavity optomechanical sensing system. *New J. Phys.* **14**, 075015 (2012).

[15] Bochmann, J., Vainsencher, A., Awschalom, D.D. & Cleland, A.N. Nanomechanical coupling between microwave and optical photons. *Nature Phys.* **9**, 712–716 (2013).

[16] Fong, K.Y., Fan, L., Jiang, L., Han, X. & Tang, H.X. Microwave-assisted coherent and nonlinear control in cavity piezo-optomechanical systems. *Phys. Rev. A* **90**, 051801 (2014).

[17] Baker, C. *et al.* Photoelastic coupling in gallium arsenide optomechanical disk resonators. *Opt. Express* **22**, 14072–14086 (2014).

[18] Balram, K.C., Davanço, M., Lim, J.Y., Song, J.D. & Srinivasan, K. Moving boundary and photoelastic coupling in gaas optomechanical resonators. *Optica* **1**, 414–420 (2014).

[19] Mauricio M. de Lima, J. & Santos, P. V. Modulation of photonic structures by surface acoustic waves.

Rep. Prog. Phys. **68**, 1639 (2005).

20 Eichenfield, M., Chan, J., Camacho, R.M., Vahala, K.J. & Painter, O. Optomechanical crystals. *Nature* **462**, 78–82 (2009).

21 Chan, J., Safavi-Naeini, A.H., Hill, J.T., Meenehan, S. & Painter, O. Optimized optomechanical crystal cavity with acoustic radiation shield. *Appl. Phys. Lett.* **101**, 081115 (2012).

22 See Supplementary Material for additional information on device fabrication, simulations of the inter-digitated transducers and phononic crystal waveguides, and measurements of acoustic wave interference effects.

23 Campbell, C.K. Applications of surface acoustic and shallow bulk acoustic wave devices. *Proc. IEEE* **77**, 1453–1484 (1989).

24 Campbell, C. *Surface acoustic wave devices for mobile and wireless communications* (Academic press, 1998).

25 Safavi-Naeini, A.H. & Painter, O. Design of optomechanical cavities and waveguides on a simultaneous bandgap phononic-photonic crystal slab. *Opt. Express* **18**, 14926–14943 (2010).

26 Tadesse, S.A. & Li, M. Sub-optical wavelength acoustic wave modulation of integrated photonic resonators at microwave frequencies. *Nature Commun.* **5** (2014).

27 Li, H., Tadesse, S.A., Liu, Q. & Li, M. Nanophotonic cavity optomechanics with propagating acoustic waves at frequencies up to 12 ghz. *Optica* **2**, 826–831 (2015).

28 Agarwal, G. & Huang, S. Electromagnetically induced transparency in mechanical effects of light. *Phys. Rev. A* **81**, 041803 (2010).

29 Weis, S. *et al.* Optomechanically Induced Transparency. *Science* **330**, 1520–1523 (2010).

30 Safavi-Naeini, A.H. *et al.* Electromagnetically induced transparency and slow light with optomechanics. *Nature (London)* **472**, 69–73 (2011).

31 Arimondo, E. *Coherent Populating Trapping in Laser Spectroscopy*, 257–354 (Elsevier Science, 1996).

32 Khan, S., Kumar, M., Chanu, S.R., Bharti, V. & Natarajan, V. Coherent population trapping (CPT) versus Electromagnetically induced transparency (EIT). *arXiv:1503.06956* (2015).

33 Wang, Y.-D. & Clerk, A.A. Using interference for high fidelity quantum state transfer in optomechanics. *Phys. Rev. Lett.* **108**, 153603 (2012).

34 Dong, C., Fiore, V., Kuzyk, M.C. & Wang, H. Optomechanical dark mode. *Science* **338**, 1609–1613 (2012).

35 Hill, J.T., Safavi-Naeini, A.H., Chan, J. & Painter, O. Coherent optical wavelength conversion via cavity

optomechanics. *Nature Commun.* **3**, 1196 (2012).

36 Liu, Y., Davanço, M., Aksyuk, V. & Srinivasan, K. Electromagnetically induced transparency and wideband wavelength conversion in silicon nitride microdisk optomechanical resonators. *Phys. Rev. Lett.* **110**, 223603 (2013).

37 Safavi-Naeini, A.H. & Painter, O. Proposal for an optomechanical traveling wave phonon-photon translator. *New J. Phys.* **13**, 013017 (2011).

38 Habraken, S., Stannigel, K., Lukin, M.D., Zoller, P. & Rabl, P. Continuous mode cooling and phonon routers for phononic quantum networks. *New J. Phys.* **14**, 115004 (2012).

39 de Lima Jr, M., Alsina, F., Seidel, W. & Santos, P. Focusing of surface-acoustic-wave fields on (100) gaas surfaces. *J. Appl. Phys.* **94**, 7848–7855 (2003).

40 Khelif, A., Choujaa, A., Benchabane, S., Djafari-Rouhani, B. & Laude, V. Guiding and bending of acoustic waves in highly confined phononic crystal waveguides. *Appl. Phys. Lett.* **84**, 4400–4402 (2004).

41 Maldovan, M. Sound and heat revolutions in phononics. *Nature* **503**, 209–217 (2013).

42 Olsson Iii, R. & El-Kady, I. Microfabricated phononic crystal devices and applications. *Measurement Science and Technology* **20**, 012002 (2009).

43 Hatanaka, D., Mahboob, I., Onomitsu, K. & Yamaguchi, H. Phonon waveguides for electromechanical circuits. *Nature Nanotech.* **9**, 520–524 (2014).

44 Mohammadi, S. & Adibi, A. On chip complex signal processing devices using coupled phononic crystal slab resonators and waveguides. *AIP Advances* **1**, 041903 (2011).

45 Metcalfe, M., Carr, S.M., Muller, A., Solomon, G.S. & Lawall, J. Resolved Sideband Emission of InAs/GaAs Quantum Dots Strained by Surface Acoustic Waves. *Phys. Rev. Lett.* **105**, 037401 (2010).

46 Fuhrmann, D.A. *et al.* Dynamic modulation of photonic crystal nanocavities using gigahertz acoustic phonons. *Nature Photon.* **5**, 605–609 (2011).

47 Yeo, I. *et al.* Strain-mediated coupling in a quantum dot-mechanical oscillator hybrid system. *Nature Nanotech.* (2013).

48 Lodahl, P., Mahmoodian, S. & Stobbe, S. Interfacing single photons and single quantum dots with photonic nanostructures. *Rev. Mod. Phys.* **87**, 347 (2015).

Author Contributions K.C.B. led the design, fabrication, and measurement of the devices, with assistance from M.D. and K.S. J.D.S. grew the epitaxial material, and K.C.B. and K.S. analyzed the data and wrote the manuscript, with input from all authors. K.S. supervised the project.

Additional Information Correspondence and requests for materials should be addressed to K.C.B. and K.S.

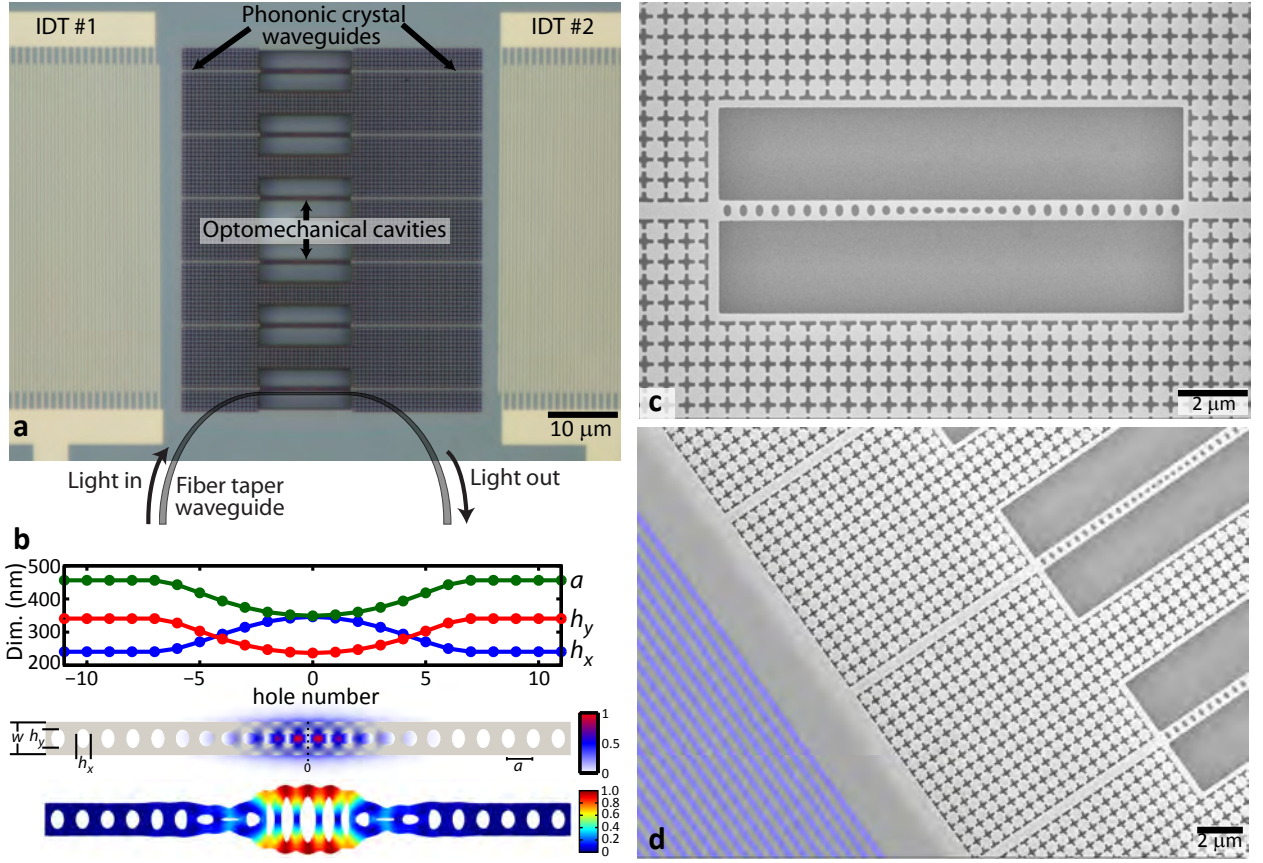**Competing financial interests** The authors declare no competing financial interests.

Figures

FIG. 1: **Piezo-optomechanical circuits.** (a) Optical micrograph of the device layout. An array of optomechanical cavities, each coupled to input and output phononic crystal waveguides, is placed between inter-digitated transducers (IDTs) that excite and/or detect surface acoustic waves. Optical coupling is done using a fibre taper waveguide, shown schematically in gray. (b) Optomechanical crystal cavity design. (Top) Variation of the lattice constant, major axis diameter, and minor axis diameter of the elliptical holes along the nanobeam; (Middle) Simulated normalized electric field amplitude for the 1550 nm optical mode. (Bottom) Simulated normalized displacement amplitude for the 2.4 GHz mechanical breathing mode. (c) Scanning electron microscope (SEM) image of a nanobeam optomechanical crystal cavity, including the adjacent input and output phononic crystal waveguides. (d) SEM image showing the transition from the input IDT (shaded in blue) to the phononic crystal waveguide and nanobeam cavity.
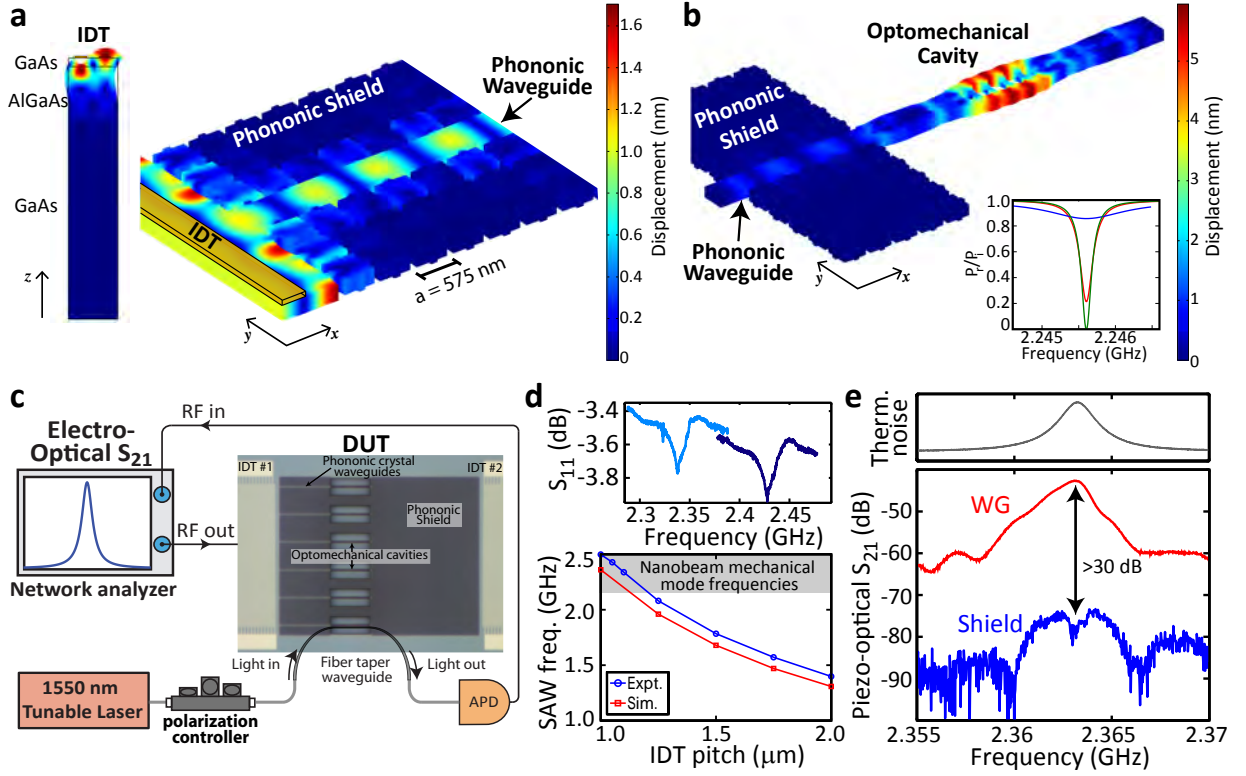
17

FIG. 2: **Coupling between propagating and localized phononic modes.** FEM simulation of (a) surface acoustic wave (SAW) generation by an IDT (left) and its propagation in a phononic crystal waveguide (right) and (b) coupling between the phononic crytsal waveguide and nanobeam cavity modes. The inset plots the acoustic reflection spectrum, for Q_m of 1.5×10^3 (blue), 1.5×10^4 (red), and 2.5×10^4 (green). (c) Setup for optical readout of the nanobeam's coherent mechanical motion, driven either through a phononic crystal waveguide (IDT 1) or a phononic shield (IDT 2). (d) (Top) IDT reflection spectrum (S_{11}) for two different finger spacings. (Bottom) Experimental (blue) and theoretical (red) IDT resonance frequency vs. IDT pitch. (e) (Top) Thermal noise spectrum of the nanobeam cavity's localized mechanical mode. The y-axis span is 10 dB. (Bottom) Coherently-detected nanobeam mechanical motion spectrum (piezo-optic S_{21}), when driven through a phononic crystal waveguide (red) and through the phononic shield (blue).
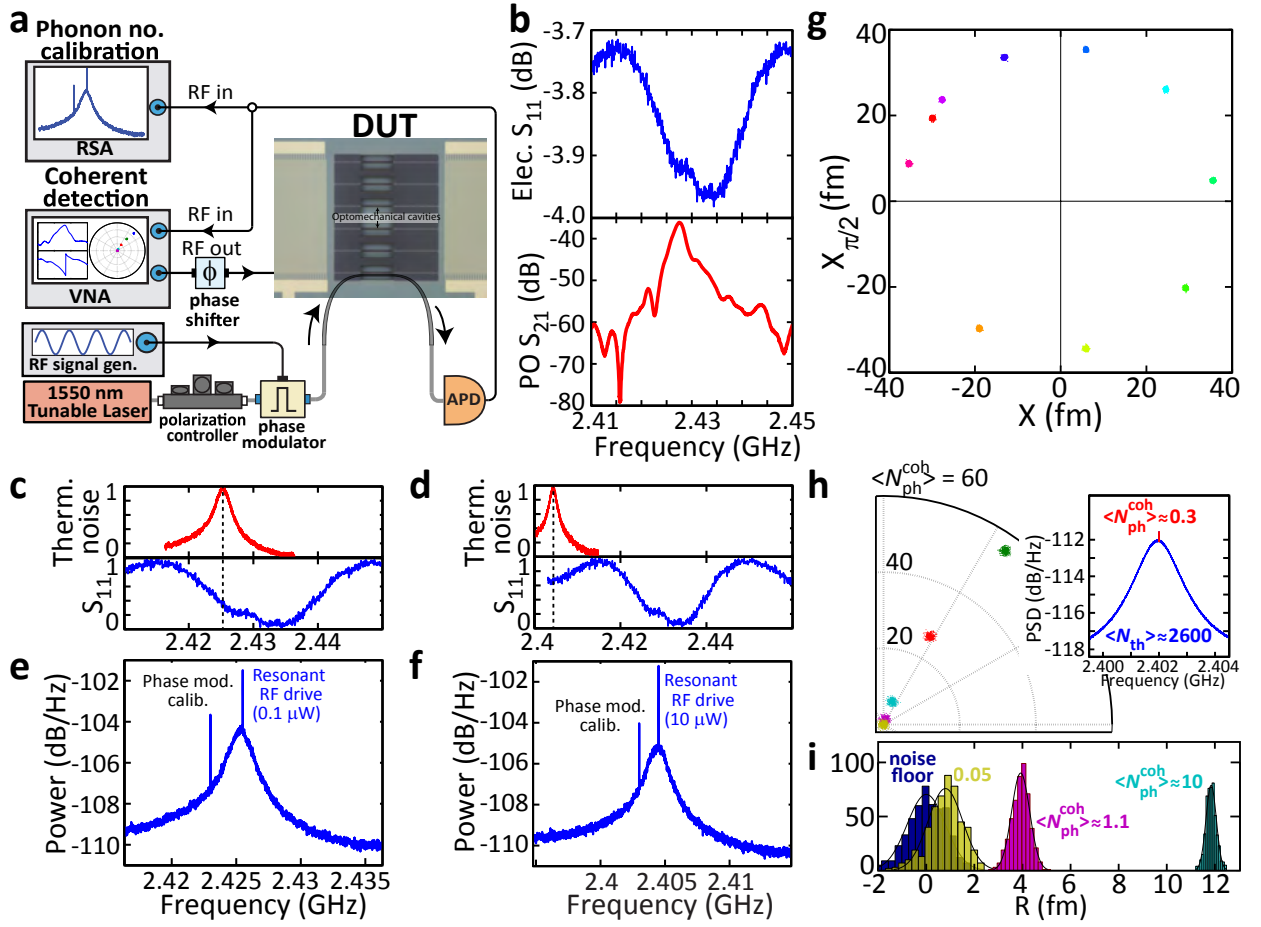
18

FIG. 3: **Acousto-optic modulation and coherent phonon detection.** (a) Setup for determining the average coherent intracavity phonon number N_{ph}^{coh} through comparison with thermal motion. (b) IDT S_{11}(top) and piezo-optic S_{21} (bottom) for a spectrally aligned IDT and nanobeam. (c)-(d) Thermal noise spectrum of the localized mechanical mode (red, RF off) and IDT S_{11} (blue) when they are spectrally (c) aligned and (d) misaligned. (e)-(f) Corresponding total photodetected spectrum (PSD) with the RF drive on, with $N_{ph}^{coh} = 43 \pm 1.5$ in (e) and $N_{ph}^{coh} = 50 \pm 1.8$ in (f). The RF power is increased by 20 dB in (f). (g) Quadrature plot with $N_{ph}^{coh} = 91 \pm 3.3$ and varying phase (measurement bandwidth = 200 Hz). (h) (Left) Polar plot of N_{ph}^{coh} with decreasing RF drive. (Right) Total PSD for $N_{ph}^{coh} = 0.3 \pm 0.01$. (i) Histogram data from (h) for small motional amplitudes (bandwidth = 20 Hz). Phonon number uncertainty (1σ) is from the combined uncertainty in sample temperature, PSD fit, and RSA error.
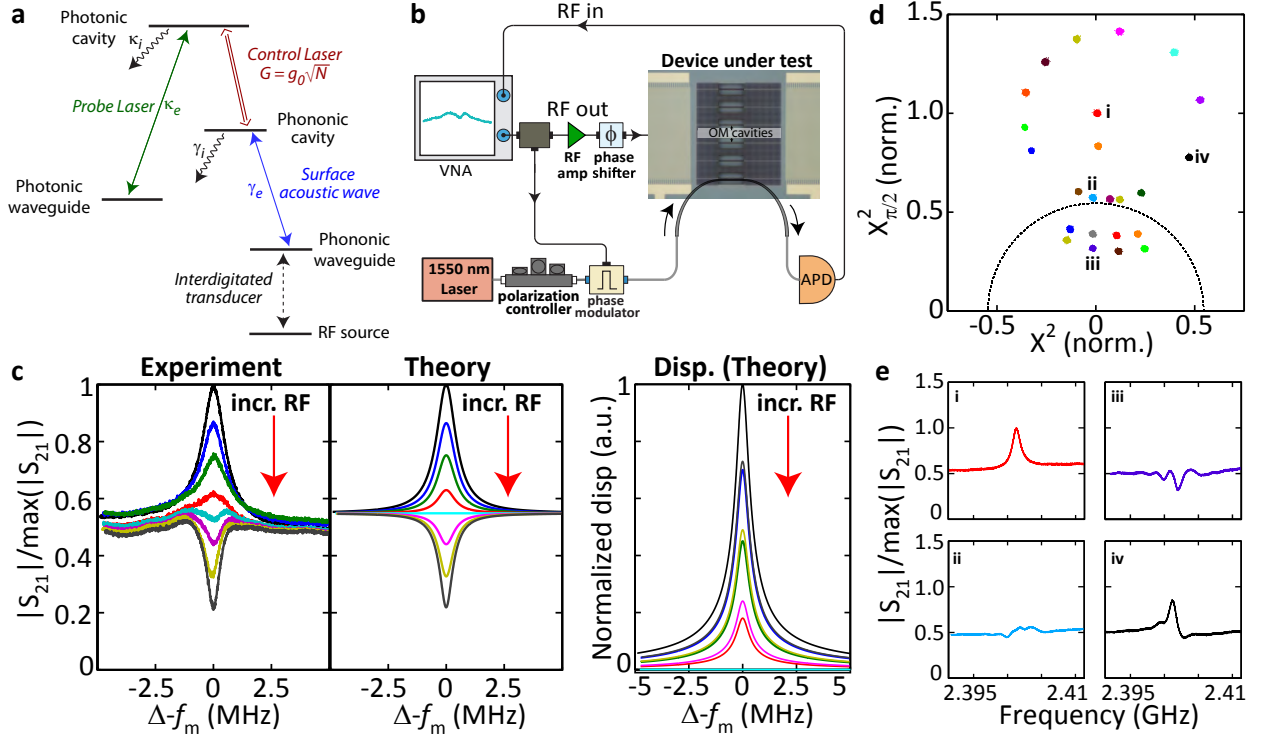
19

FIG. 4: **Acoustic wave interference**. (a) Level diagram indicating the phononic cavity population driven either optically or via RF-generated propagating acoustic waves. (b) Experimental setup. The VNA output is split and one part is sent to an electro-optic phase modulator for optically driving the phononic cavity. The other part is phase shifted, amplified, and sent to the IDT for an RF-generated acoustic wave drive. (c) Transmitted probe sideband spectrum as a function of RF power showing optomechanically-driven motion (RF = 0) (black), acoustic wave interference (cyan), and RF-dominated motion (dark gray) regimes (Experimental data on left, theory in center, and simulated cavity displacement on the right). (d) Coherent motion in phase space (bandwidth = 200 Hz). The black dashed semicircle is the off-resonance background. The four numbered points, with frequency response curves shown in (e), correspond to (i) optomechanically-driven motion, (ii) acoustic wave interference, (iii) RF-dominated motion, and (iv) Fano lineshape behaviour.

20

Supplementary Information for Coherent coupling between radio frequency, optical, and acoustic waves in piezo-optomechanical circuits

Krishna C. Balram,[1,2,*] Marcelo I. Davanço,[1] Jin Dong Song,[3] and Kartik Srinivasan[1,†]

[1]*Center for Nanoscale Science and Technology, National Institute of Standards and Technology, Gaithersburg, MD 20899, USA*
[2]*Maryland NanoCenter, University of Maryland, College Park, MD 20742, USA*
[3]*Center for Opto-Electronic Materials and Devices Research,*
Korea Institute of Science and Technology, Seoul 136-791, South Korea

I. FABRICATION PROCEDURE

The epitaxial material used in this work consists of a 220 nm thick GaAs layer on a 1.5 μm thick $Al_{0.7}Ga_{0.3}As$ sacrificial layer. The samples were spin-coated with positive tone electron beam resist and baked at 180 °C for 120 s. The IDT patterns were exposed in a 100 keV direct write electron beam lithography system with a beam current of 2 nA and nominal dose of 580 μC/cm^2. After exposure, the electron beam resist was developed using MIBK:IPA 1:3 solution (90 s). To remove residual undeveloped resist, the samples were exposed to an O_2 plasma (6.7 Pa = 50 mTorr, 75 W) for 5 s. The IDT metallization was carried out in an electron beam evaporator with the metal stack Cr (5 nm)/Pt (15 nm)/Au (30 nm) deposited in succession. The lift-off was carried out by soaking the samples overnight in acetone and using gentle sonication.

For the nanobeam overlay, the samples were spin-coated with positive tone electron beam resist and baked at 180 °C for 120 s. The nanobeam patterns were exposed in a 100 keV direct write electron beam lithography system with a beam current of 200 pA and nominal dose of 250 μC/cm^2. The nanobeam patterns were aligned to the IDT using alignment marks that were exposed along with the IDTs. After exposure, the electron beam resist was developed using hexyl acetate (65 s). To remove residual undeveloped resist, the samples were exposed to an O_2 plasma (6.7 Pa = 50 mTorr, 75 W) for 10 s. The nanobeam patterns were then transferred to the underlying GaAs layer using an inductively coupled plasma reactive ion etcher with an Ar/Cl_2 chemistry. The electron beam resist was stripped using trichloroethylene, and the nanobeams were undercut with a timed wet etch using either concentrated (49 %) HF solution or $(NH_4)_2S$ and dilute HF (50:1 volume dilution in H_2O).

II. SAW RESONANCE SIMULATION

To calculate the resonance frequency for surface acoustic waves for our material stack, we model a one wavelength width cross-section of the stack with periodic boundary conditions and solve for the resonance frequency of the stack. We used the following parameters to model $Al_xGa_{1-x}As$ with $x = 0.7$: $e_{14} = -0.16 - 0.065x$ C/m^2, $C_{11} = (118.8 + 1.4x)$ GPa, $C_{12} = (53.8 + 3.2x)$ GPa and $C_{44} = (59.4 - 0.5x)$ GPa[1]. The calculated frequencies are uniformly lower than the measured frequencies, which we attribute to imperfect knowledge of the density and thickness of the metallic stack (Cr/Pt/Au) comprising the IDT.

III. FREQUENCY RESPONSE ANALYSIS FOR ACOUSTIC MODE COUPLING

For the simulation results shown in Figure 2(b) in the main text, the surface acoustic wave was launched by applying a prescribed displacement of 1 nm (the simulation was linear in displacement, the starting displacement amplitude is arbitrary) in the x-direction to the end facet of the line-defect waveguide (x is the direction of wave propagation). The x-displacement is chosen so as to launch a symmetric Lamb wave in the defect waveguide and nanobeam that has the right z-symmetry to couple to the nanobeam breathing mode.

To calculate the coupling efficiency shown in Figure 2(b) we define the acoustic Poynting vector (P_j)

$$P_j = \frac{1}{2}Re(-T_{ij}v_i^*) \tag{S1}$$

where T_{ij} is the stress and v_i is the particle velocity. The reflection spectrum is calculated by doing two simulations, one with the nanobeam cavity and a second with a bare waveguide whose width is equal to that of the nanobeam cavity. The Poynting vector is calculated at the input port of the cavity and the reflected power is defined as:

$$R = 1 - \frac{P_{\text{trans,cav}}}{P_{\text{trans,wvg}}} \tag{S2}$$

where the transmitted powers ($P_{\text{trans,cav}}$ and $P_{\text{trans,wvg}}$) are all calculated in the direction of the propagating mode (x).

IV.   NANOBEAM BREATHING MODE FREQUENCY DEPENDENCE ON WIDTH

To ensure that the resonance frequency of the nanobeam optomechanical cavity's mechanical breathing mode lies within the excitation bandwidth of the IDT, we excite an array of cavities with varying beam width with the same IDT. Figure S1(a) shows the dependence of the breathing mode frequency on the width of the nanobeam and indicates that a 40 nm tuning in the width results in an approximately 155 MHz tuning in breathing mode frequency. In fabricated devices, the width of the individual beams within the nanobeam array is varied in 5 nm steps.
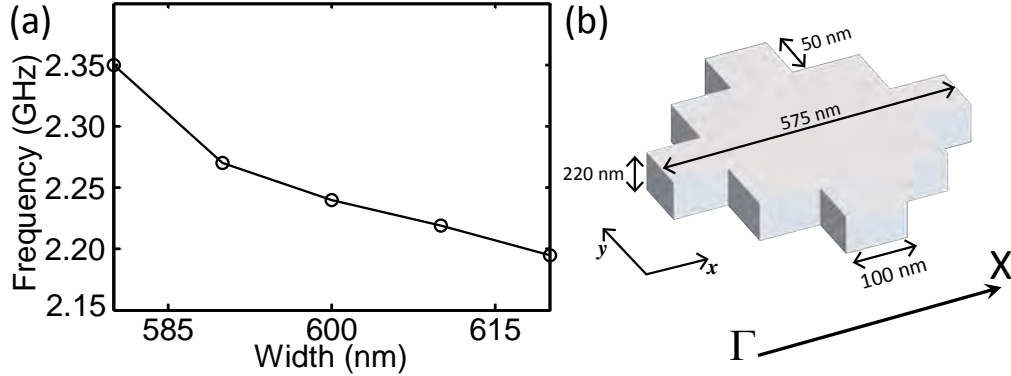

FIG. S1: (a) Calculated nanobeam optomechanical crystal cavity mechanical breathing mode frequency as a function of beam width. (b) Schematic of the unit cell of the phononic shield showing the different dimensions.

V.   PHONONIC SHIELD BAND STRUCTURE

The dispersion diagram for acoustic wave propagation in the Γ-X direction for the phononic shield (whose unit cell is shown in Figure S1(b)) is shown in Figure S2. The modes of a unit cell with periodic boundary conditions in the propagation direction (Γ-X) were calculated using a finite-element solver to determine the dispersion diagram. The modes are classified as odd / even according to the symmetry in the out of plane (z) direction. GaAs is modelled as an orthotropic elastic material with parameters $E_x = 121.2$ GPa, $E_y = 121.2$ GPa, $E_z = 85.9$ GPa, $\nu_{xy} = 0.0209$, $\nu_{yz} = 0.4434$, $\nu_{xz} = 0.312$, $G_{xy} = 32.5$ GPa, $G_{yz} = 59.4$ GPa, and $G_{xz} = 59.4$ GPa.

We note that a wide variety of phononic shield structures based on circular / square holes have been studied[2–5]. For the GaAs material system, achieving a complete bandgap within such geometries necessitates high hole filling fractions, and in the 2.4 GHz frequency range this requires patterning dimensions at the sub-25 nm length scale, making fabrication challenging. The advantage of the cross structure is that it allows one to achieve a complete acoustic band-gap with minimum feature size of 100 nm, which can be easily obtained by standard electron-beam lithography.

VI.   BASIC OPTOMECHANICAL SPECTROSCOPY

Figure S3(a) shows the optical transmission spectrum of the device in Figure 3(g)-(h) and Figure 4 (main text) whose $Q_{opt} = 36600 \pm 400$ (uncertainty from the 95 % confidence interval of a Lorentzian fit to the data). Figure S3(b) shows the corresponding thermal noise spectrum for the localized mechanical mode with $Q_m = 1400 \pm 5$ (uncertainty from the 95 % confidence interval of a Lorentzian fit to the data). The optomechanical coupling rate $g_0/2\pi$ for the device was measured to be 1.1 MHz $\pm$ 60 kHz using the procedure discussed below.
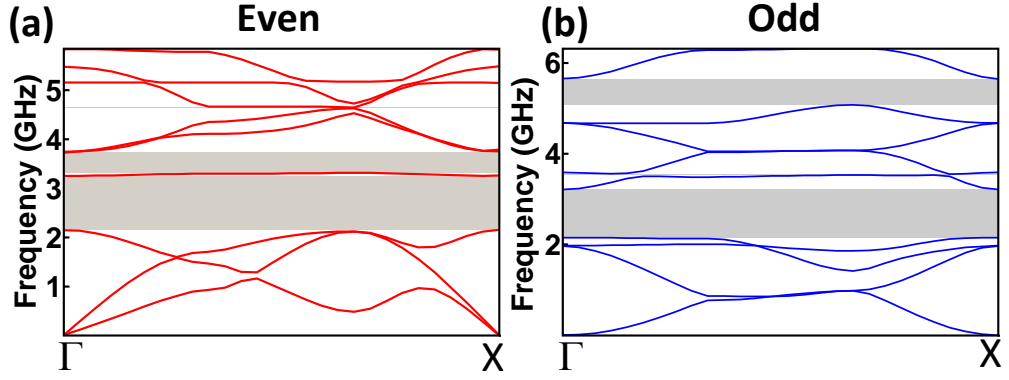
FIG. S2: Calculated phononic bandstructure for acoustic waves with (a) even and (b) odd symmetry in the out-of-plane direction (z), propagating along the Γ-X direction in the phononic shield. The presence of a complete bandgap for the frequencies of interest (2.25 GHz to 2.75 GHz) is clearly seen.
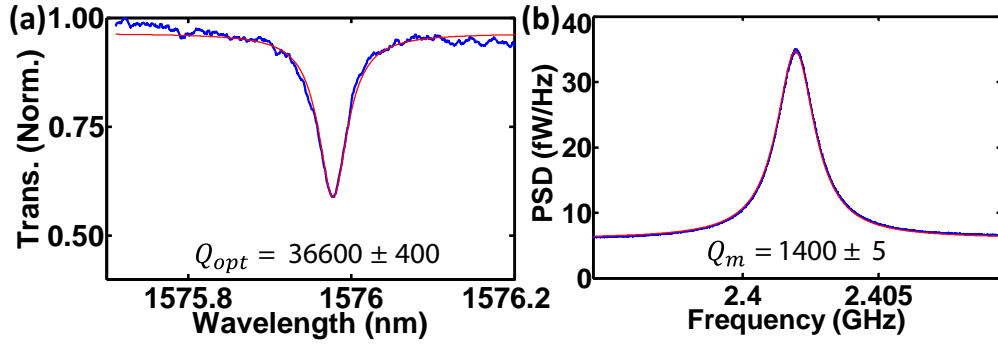

FIG. S3: (a) Transmission spectrum of the cavity optical mode. (b) Thermal noise power spectral density (PSD) of the nanobeam breathing mode (as measured on the RSA). Blue curves represent experimental data, Red: Lorentzian fits. The uncertainty in the optical and mechanical quality factors represent Lorentzian fit uncertainty, 95 % confidence intervals.

VII. g_0 CALIBRATION USING AN ELECTRO-OPTIC PHASE MODULATOR

We use a phase modulator to calibrate the optomechanical coupling rate g_0[6,7]. The basic idea is to relate the modulation produced by sending light through the cavity optomechanical system (which is driven by its contact with the thermal environment) to a direct phase modulation applied with an electro-optic phase modulator. Because both undergo the same transduction function, the ratio of the integrated power in their photocurrent RF spectra will be related to the ratio of g_0 and the phase modulator's modulation index. We go through this derivation below.

The root-mean-square (rms) thermal displacement amplitude (α_{thermal}) is related to the temperature (T) using the equipartition theorem:

$$\frac{1}{2}m_{\text{eff}}\Omega_m^2\alpha_{\text{thermal}}^2 = \frac{1}{2}k_{\text{B}}T \tag{S3}$$

where m_{eff} is the motional mass of the resonator and Ω_{m} is the mechanical mode frequency. We define a thermal modulation index:

$$\beta_{\text{thermal}} = \frac{\alpha_{\text{thermal}}g_{\text{om}}}{\Omega_{\text{m}}} \tag{S4}$$

where the optomechanical coupling parameter (g_{om}) is defined by:

$$\omega(\alpha) = \omega_0 + g_{\text{om}}\alpha \tag{S5}$$

with ω_0 being the unperturbed cavity frequency. This leads to:

$$\beta_{\text{thermal}}^2 = \frac{k_{\text{B}}T}{m_{\text{eff}}\Omega_{\text{m}}^2}\frac{g_{\text{om}}^2}{\Omega_{\text{m}}^2} \tag{S6}$$

The optomechanical coupling rate g_0 is:

$$g_0 = g_{\text{om}}x_{\text{zpf}} \tag{S7}$$

where the (rms) amplitude of the zero point fluctuation is:

$$x_{\text{zpf}} = \sqrt{\frac{\hbar}{2m_{\text{eff}}\Omega_{\text{m}}}} \tag{S8}$$

which can be directly calculated as $\sqrt{\langle 0|\, x^2\,|0\rangle}$ from the ground state wavefunction $|0\rangle$ of the simple harmonic resonator.
We then relate g_0 to β_{thermal}:

$$\beta_{\text{thermal}}^2 = \frac{2k_{\text{B}}T}{\hbar\Omega_{\text{m}}^3}g_0^2 \tag{S9}$$

The modulation index (β_{pm}) of the phase modulator is defined as:

$$\beta_{\text{pm}} = \frac{\pi V_{\text{sig}}}{V_\pi} \tag{S10}$$

where V_{sig} is the signal amplitude and V_π is the modulator half wave voltage.

By comparing the (integrated) powers in the cavity mechanical mode signal ($S_{\text{cav}}(\Omega_{\text{m}})$) and the phase modulator signal ($S_{\text{pm}}(\Omega_{\text{pm}})$) obtained from the electronic spectrum analyzer, we get:

$$g_0^2 = \frac{\hbar\Omega_{\text{m}}}{2k_{\text{B}}T}\Omega_{\text{m}}^2\beta_{\text{pm}}^2\frac{S_{\text{cav}}(\Omega_{\text{m}})}{S_{\text{pm}}(\Omega_{\text{pm}})} \tag{S11}$$

VIII. EXTRACTING CAVITY DISPLACEMENT AND PHONON NUMBER DUE TO EXCITATION VIA THE PHONONIC WAVEGUIDE

The modulation index due to the propagating wave β_{saw} is given by:

$$\beta_{\text{saw}} = \frac{\alpha_{\text{cav}}g_{\text{om}}}{\Omega_{\text{saw}}} \tag{S12}$$

wherein α_{cav} is the cavity displacement (rms) due to the coupling from the propagating acoustic wave.

To extract the average coherent intracavity phonon number $N_{\text{ph}}^{\text{coh}}$, we compare the area under the coherent acoustic wave peak with the integrated area of the mechanical mode thermal noise spectrum, noting that the average thermal phonon occupation number is given by $N_{th} \approx k_{\text{B}}T/\hbar\Omega_{\text{m}}$

$$N_{\text{ph}}^{\text{coh}} = \frac{k_{\text{B}}T}{\hbar\Omega_{\text{m}}}\frac{S_{\text{coh}}(\Omega_{\text{coh}})}{S_{\text{th}}(\Omega_m)} \tag{S13}$$

We can now relate the cavity's coherent rms displacement amplitude α_{cav} to N_{ph}^{coh} using:

$$N_{\text{ph}}^{\text{coh}}\hbar\Omega_{\text{m}} = m_{\text{eff}}\Omega_m^2\alpha_{\text{cav}}^2 \tag{S14}$$

which can be re-written as:

$$N_{\text{ph}}^{\text{coh}} = \frac{1}{2}\left(\frac{\alpha_{\text{cav}}}{x_{\text{zpf}}}\right)^2 \tag{S15}$$

where we have substituted $x_{\text{zpf}} = \sqrt{\frac{\hbar}{2m_{\text{eff}}\Omega_{\text{m}}}}$.

IX.   ACOUSTO-OPTIC MODULATOR V_π CALCULATION

To determine the equivalent V_π of our piezo-optomechanical circuits when considering them to operate as an acousto-optic phase modulator, we use the relationship:

$$V_\pi = \pi \frac{V_{\mathrm{saw}}}{\beta_{\mathrm{saw}}} \tag{S16}$$

To determine V_{saw}, the applied RF voltage that is converted to a propagating surface acoustic wave, we use the resonant dip in the S_{11} spectrum of our IDT to determine the transmitted RF power (in our case -0.25 dB) and assume a 50 Ω load to determine the corresponding voltage. The modulation index due to the SAW is extracted using the procedure described in the previous section.

X.   EFFICIENCY ENHANCEMENT FOR RESONANT ACOUSTO-OPTIC MODULATORS

We can use the equations of temporal coupled mode theory developed for photonics to study acoustic wave interaction with optomechanical cavities. In this case, we assume the mechanical resonator is coupled to both input and output waveguides and is excited with an acoustic wave from the input waveguide:

$$\frac{db}{dt} = -i\Omega_m b - \frac{b}{\tau_i} - \frac{2b}{\tau_c} + \sqrt{\frac{2}{\tau_c}} b_{in} \tag{S17}$$

wherein b is the mechanical displacement amplitude, τ_i represents the intrinsic cavity (amplitude) decay time constant, and τ_c the waveguide cavity coupling time constant.

Assuming a solution of the form $be^{-i\Omega t}$, we can solve for the steady-state cavity energy:

$$\frac{|b|^2}{|b_{in}|^2} = \frac{\frac{2}{\tau_c}}{(\Omega - \Omega_m)^2 + (\frac{1}{\tau_i} + \frac{2}{\tau_c})^2} \tag{S18}$$

We can rewrite the equations using the intrinsic and coupling quality factors ($Q_{i,c} = \frac{\Omega_m \tau_{i,c}}{2}$) and solve for the steady-state cavity energy ($\Omega_m |b|^2$), with the input power normalized as $|b_{in}|^2 = 1$:

$$\frac{\Omega_m |b|^2}{|b_{in}|^2} = \frac{Q_i^2 Q_c}{(2Q_i + Q_c)^2} \tag{S19}$$

For the case of critical coupling $Q_i = Q_c = Q$, this reduces to:

$$\frac{\Omega_m |b|^2}{|b_{in}|^2} = \frac{Q}{9} \tag{S20}$$

This equation is consistent with the steady-state cavity energy being enhanced by the mechanical resonator's quality factor. For resonant acousto-optic phase modulator applications, we are more interested in the steady-state cavity displacement and this will scale as $\sqrt{Q}$, and thus the voltage required to achieve a certain phase shift, which scales linearly with displacement, will also scale as $\sqrt{Q}$.

XI.   ACOUSTIC WAVE INTERFERENCE FROM TWO IDTS

The main text discusses acoustic wave interference that occurs when the mechanical mode is driven optically and electrically with equal amplitude and opposite phase. The same phenomenon occurs when the mechanical resonator is pumped by two IDTs through two phononic waveguides with equal amplitudes and opposite phase. To demonstrate this, we use the device shown in Figure 3(a) in the main text, and modify the experimental setup of Figure 2(c) so that the output of the VNA is split in two, with each path fed to its own RF amplifier and then connected to an IDT. The resulting data is presented in Figure S4. The two IDTs when turned on alone (ii and iii in the polar plot) result in a regular electro-optic S_{21} measurement as in Figure 2(e), for example. The asymmetry between the spectral

responses can be attributed to fabrication-induced asymmetry in the device and the asymmetric coupling induced due to the fiber taper touching down on the device. When the two IDTs are both fed by an RF signal with a varying phase difference, one can sweep out a circular trajectory in phase space. The intersection of this circle with the origin corresponds to the acoustic wave cancellation condition. The mechanical resonator is loaded in a dark state by the destructive interference between the excitation amplitudes of the two IDTs. For an arbitrary phase difference between the two IDTs, the response in general has an asymmetric Fano-like lineshape.
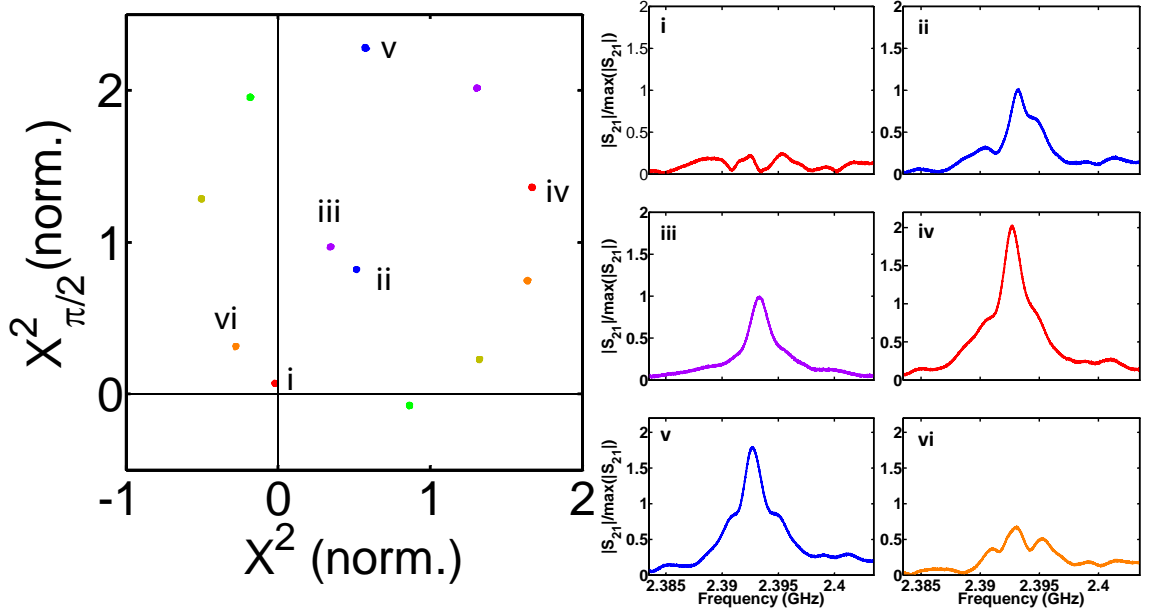

FIG. S4: Phase space diagram for different values of the RF amplitude and phase for a nanobeam optomechanical crystal cavity pumped by two phononic waveguides, each of which is sourced by its own IDT. The six numbered points, with frequency response curves shown in the side panel, correspond to (i) acoustic wave cancellation, (ii) IDT 1 ON, IDT 2 OFF, (iii) IDT 1 OFF, IDT 2 ON, and (iv, v and vi) Fano lineshape behavior for varying phase difference between IDT 1 and IDT 2. The measurement bandwidth in these experiments is 200 Hz.

XII.   ACOUSTIC WAVE INTERFERENCE THEORY

The Hamiltonian for the optically and acoustically driven cavity optomechanical system can be written:

$$H_{sys} = H_{photons} + H_{phonons} + H_{int} + H_{opt,drive} + H_{acoustic,drive} \tag{S21}$$

wherein the different contributing terms can be written as:

$$H_{photons} = \hbar(a^\dagger a + \frac{1}{2}) \tag{S22}$$

$$H_{phonons} = \hbar(b^\dagger b + \frac{1}{2}) \tag{S23}$$

$$H_{int} = \hbar g_0 a^\dagger a(b + b^\dagger) \tag{S24}$$

$$H_{opt,drive} = i\hbar\sqrt{\frac{\kappa_e}{2}}(a_{in}(t)a^\dagger - a_{in}^\dagger(t)a) \tag{S25}$$

$$H_{acoustic,drive} = i\hbar\sqrt{\frac{\gamma_e}{2}}(b_{in}(t)b^\dagger - b_{in}^\dagger(t)b) \tag{S26}$$

The coupled equations of motion for the intracavity optical field amplitude and the cavity mechanical displacement amplitude derived from the Hamiltonian are:

$$\dot{a} = -(i\Delta + \frac{\kappa_i}{2})a - ig_0a(b + b^\dagger) - \sqrt{\frac{\kappa_e}{2}}a_{in} \tag{S27}$$

$$\dot{b} = -(i\Omega_{\mathrm{m}} + \frac{\gamma_i}{2})b - ig_0a^\dagger a - \sqrt{\frac{\gamma_e}{2}}b_{in} \tag{S28}$$

with $a(a^\dagger)$ representing the annihilation (creation) operator for the intracavity optical field, $b(b^\dagger)$ the annihilation (creation) operator for the mechanical displacement. Δ represents the detuning of the control beam from the optical cavity resonance frequency, κ_i the intrinsic decay rate of the optical cavity, and κ_e is the extrinsic decay rate (coupling rate) to the waveguide. Ω_m represents the mechanical mode frequency, γ_i the intrinsic decay rate of the mechanical cavity and γ_e is the extrinsic decay rate (coupling rate) to the phononic waveguide. a_{in} and b_{in} represent the optical and acoustic field strengths in the photonic and phononic waveguides respectively. g_0 represents the vacuum optomechanical coupling rate.

We make the following ansatz:

$$a \Rightarrow \alpha = \alpha_0 + \alpha_{d+}e^{-i\Omega_d t} + \alpha_{d-}e^{i\Omega_d t} \tag{S29}$$

$$b \Rightarrow \beta = \beta_0 + \beta_{d+}e^{-i\Omega_d t} \tag{S30}$$

Physically, this ansatz correponds to linearizing around the steady-state photon (α_0) and phonon (β_0) amplitudes. For the mechanical motion:

$$\beta_{d-} = \beta_{d+}^* \tag{S31}$$

Substituting equations S29 and S30 into equation S28 and collecting terms at DC:

$$\beta_0 = \frac{-ig_0|\alpha_0|^2}{i\Omega_m + \frac{\gamma_i}{2}} \tag{S32}$$

The true numerator is $-ig_0(|\alpha_0|^2 + |\alpha_{d+}|^2 + |\alpha_{d-}|^2)$ but we neglect the latter two terms under the assumption that $|\alpha_0|^2 >> |\alpha_{d+}|^2 + |\alpha_{d-}|^2$.

We can write the incident acoustic displacement as:

$$\beta_{in} = \beta_{in,0}e^{i\psi} \tag{S33}$$

wherein $\beta_{in,0}$ is the amplitude of the incident acoustic wave and ψ represents the (variable) phase difference between the RF signal applied to the phase modulator (PM) and the IDT.

Substituting equations S29 and S30 into equation S28 and collecting terms at $e^{-i\Omega_d t}$:

$$\beta_{d+} = \frac{-ig_0(\alpha_0\alpha_{d-}^* + \alpha_{d+}\alpha_0^*) - \sqrt{\frac{\gamma_e}{2}}\beta_{in,0}e^{i\psi}}{i(\Omega_m - \Omega_d) + \frac{\gamma_i}{2}} \tag{S34}$$

We can now see that the mechanical resonator's coherent amplitude β_{d+} is driven optomechanically, through beating of the pump (α_0) and probe sidebands (α_{d+} and α_{d-}), as well as through the phononic channel by β_{in}. When the amplitude of these two terms is equal, the phase ψ can be tuned to achieve cancellation with β_{d+}=0, corresponding to the acoustic coherent population trapping condition.

Having determined an equation for the mechanical resonator's coherent displacement amplitude, we now consider the system's optical response. The input field can be written as:

$$\alpha_{in} = \alpha_{in,0}(1 + i\frac{\phi}{2}e^{i\Omega_d t} + i\frac{\phi}{2}e^{-i\Omega_d t}) \tag{S35}$$

where ϕ is the modulation index that represents the action of the optical phase modulator on the input optical pump field.

Substituting equations S29 and S30 into equation S27 and collecting terms at DC:

$$\alpha_0 = -\frac{\sqrt{\frac{\kappa_e}{2}}\alpha_{in,0}}{i(\Delta + 2g_0(\beta_0 + \beta_0^*)) + \frac{\kappa_i}{2}} \tag{S36}$$

Substituting equations S29 and S30 into equation S27 and collecting terms at $e^{-i\Omega_d t}$:

$$\alpha_{d+} = \frac{-2ig_0\alpha_0\beta_{d+} - \sqrt{\frac{\kappa_e}{2}}\alpha_{in,+}}{i(\Delta - \Omega_d) + \frac{\kappa_i}{2}} \tag{S37}$$

Substituting equations S29 and S30 into equation S27 and collecting terms at $e^{i\Omega_d t}$:

$$\alpha_{d-} = \frac{-2ig_0\alpha_0\beta_{d+}^* - \sqrt{\frac{\kappa_e}{2}}\alpha_{in,-}}{i(\Delta + \Omega_d) + \frac{\kappa_i}{2}} \tag{S38}$$

The two sidebands at the output are:

$$|\alpha_{d+,out}| = |\alpha_{d,in+} + \sqrt{\frac{\kappa_e}{2}}\alpha_{d+}| \tag{S39}$$

$$|\alpha_{d-,out}| = |\alpha_{d,in-} + \sqrt{\frac{\kappa_e}{2}}\alpha_{d-}| \tag{S40}$$

In the resolved sideband case (when the pump is blue-detuned), we can derive a condition for observing acoustic wave interference. The relevant equations, in the limit that only the α_{d-} sideband and β_{d+} matter, are:

$$\beta_{d+} = \frac{-ig_0(\alpha_0\alpha_{d-}^*) - \sqrt{\frac{\gamma_e}{2}}\beta_{in,0}e^{i\psi}}{i(\Omega_{\mathrm{m}} - \Omega_d) + \frac{\gamma_i}{2}} \tag{S41}$$

$$\alpha_{d-} = \frac{-2ig_0\alpha_0\beta_{d+}^* - \sqrt{\frac{\kappa_e}{2}}\alpha_{in,-}}{i(\Delta + \Omega_d) + \frac{\kappa_i}{2}} \tag{S42}$$

Acoustic coherent population trapping corresponds to $\beta_{d+} = 0$. In this limit, α_{d-} reduces to:

$$\alpha_{d-} = \frac{-\sqrt{\frac{\kappa_e}{2}}\alpha_{in,-}}{i(\Delta + \Omega_d) + \frac{\kappa_i}{2}} \tag{S43}$$

If we substitute this back in equation S41, we get the condition for the amplitude and phase of the propagating acoustic wave input to engineer acoustic coherent population trapping:

$$\sqrt{\frac{\gamma_e}{2}}\beta_{in,0}e^{i\psi} = -ig_0\alpha_0\alpha_{d-}^* \tag{S44}$$

Substituting α_{d-} from equation S42 leads us to:

$$\sqrt{\frac{\gamma_e}{2}}\beta_{in,0}e^{i\psi} = \frac{-i\sqrt{\frac{\kappa_e}{2}}g_0\alpha_0\alpha_{in,-}^*}{-i(\Delta + \Omega_d) + \frac{\kappa_i}{2}} \tag{S45}$$

XIII. COMPARISON BETWEEN OMIT, EMIT, AND ACOUSTIC WAVE INTERFERENCE

A number of different coherent interference effects have been observed in cavity optomechanical systems, and more recently [8–10], in piezoelectrically actuated cavity optomechanical systems [11,12]. Here, we compare these different effects with those observed in our experiments. A key conclusion is that while these previous demonstrations have involved interference in the optical domain, the acoustic coherent population trapping effect we have observed is a novel cancellation occuring in the mechanical domain.

Figure S5 schematically depicts four different physical situations: (a) waveguide-cavity coupling in a system without any optomechanical interaction; (b) optomechanically-induced transparency [8–10]; (c) electromechanically-induced optical transparency (EMIT) or microwave-assisted OMIT [11,12]; and (d) acoustic coherent population trapping. The pump is detuned one mechanical resonance away from the optical cavity line-center and we monitor the probe transmission by looking at the coherent RF spectrum of the photodetected signal (generated by the beating between the pump and the probe) transmitted past the cavity. We assume that the system is sideband-resolved, so that only one of the sidebands produced by the phase modulator interacts with the cavity. Our system is sufficiently close to the sideband-resolved regime ($\kappa_{opt}/2\pi \approx 5.2$ GHz, $\Omega_\mathrm{m}/2\pi \approx 2.4$ GHz) for this assumption to be largely valid. While the calculations presented in the main text account for only one sideband, we have verified that including both sidebands does not change the qualitative nature of the results.

Starting with a simple side-coupled waveguide cavity system (assuming no optomechanical coupling), an incident optical probe will show a characteristic Lorentzian dip in its transmission spectrum corresponding to the optical cavity resonance (shown in Figure S5(a)). If we now turn the optomechanical coupling on, when the frequency difference between the pump and the probe approaches the mechanical resonance frequency, their interference drives the mechanical motion of the cavity and scatters photons from the pump to the probe beam frequency. These additional probe photons can interfere either constructively or destructively (depending on the pump detuning) with the transmitted probe beam (from the regular waveguide-cavity scenario) and leads to the opening of a transparency window in the transmission spectrum (Figure S5(b)), a process commonly referred to as optomechanically induced transparency (OMIT)[9,10]. It is important to keep in mind that the interference occurs in the optical domain and the mechanical mode is coherently driven (has a non-zero displacement amplitude).

To observe OMIT, the optomechanical coupling rate $g_0/2\pi$ has to be sufficiently strong so that the beating between the pump and probe can drive the mechanical motion with sufficient amplitude to scatter photons from the pump to the probe beam frequency. In systems with small $g_0/2\pi$, the mechanical motion can be coherently driven by a different mechanism (usually by acoustic waves using the piezoelectric effect) and as long as the RF signal driving the mechanics is derived from the same source as the signal driving the electro-optic phase modulator, the photons scattered by the resonator from the pump will be phase coherent with the probe photons and one can see the induced transparency effect (Figure S5(c)). This has been referred to as electromechanically induced transparency or microwave-assisted transparency in the literature[11,12]. In effect, it is not different from OMIT, except the source driving the coherent mechanical motion is electrical rather than optical, and the character of the interference (constructive, destructive, or Fano-like) is set by the relative phase between the electrical drive and optical probe.

Finally, in a system with both strong $g_0/2\pi$ and electrical drive, as we have presented in this work, the mechanical resonator can be driven both optically (due to the beating between pump and probe, like in OMIT) or electrically (like in EMIT). By choosing the amplitude and the phase of the electrical drive, one can see either constructive or destructive interference in the mechanical domain (Figure S5(d)). Unlike pure OMIT / EMIT, the interference actually occurs in the acoustic domain and in case of destructive interference, the coherent component of the mechanical motion is zero. In this case, the system shows coherent population trapping for phonons analogous to the CPT observed in atomic systems. One can also say that the system has reached a mechanically 'dark' state, and the transmission goes back to that of a bare optical waveguide-cavity system.

The term 'coherent population trapping' was chosen because the overall system, schematically depicted in Figure 4a and re-displayed in Figure S6(a), can be viewed from the perspective of the phononic cavity as an effective three-level system, in which the phononic cavity is populated through either an optomechanically-mediated path or an RF-driven path (Figure S6(b)). The mechanical dark state - cancellation of the phononic cavity's coherent mechanical motion - occurs when the strength of the two transitions is equal (and phase is opposite). This is analogous to the situation in atomic physics, where coherent population trapping refers to an interference occuring when the two terms are equal in amplitude, while EIT is used when the control field is much stronger than the probe field [13,14].

The analogy between acoustic CPT and the coherent population trapping effect observed in atomic systems is not perfect. For example, in atomic systems, one is able to establish coherence between the two ground states of the system via the application of the two strong control fields. In our system, the effective ground states are not discrete but involve a continuum of states, due to the contact with the photonic and phononic waveguides, respectively. Given the fast decay channels associated with this coupling, we do not expect to reproduce the full variety of behaviors observed in the atomic systems, and of course, all effects we have observed are purely classical.
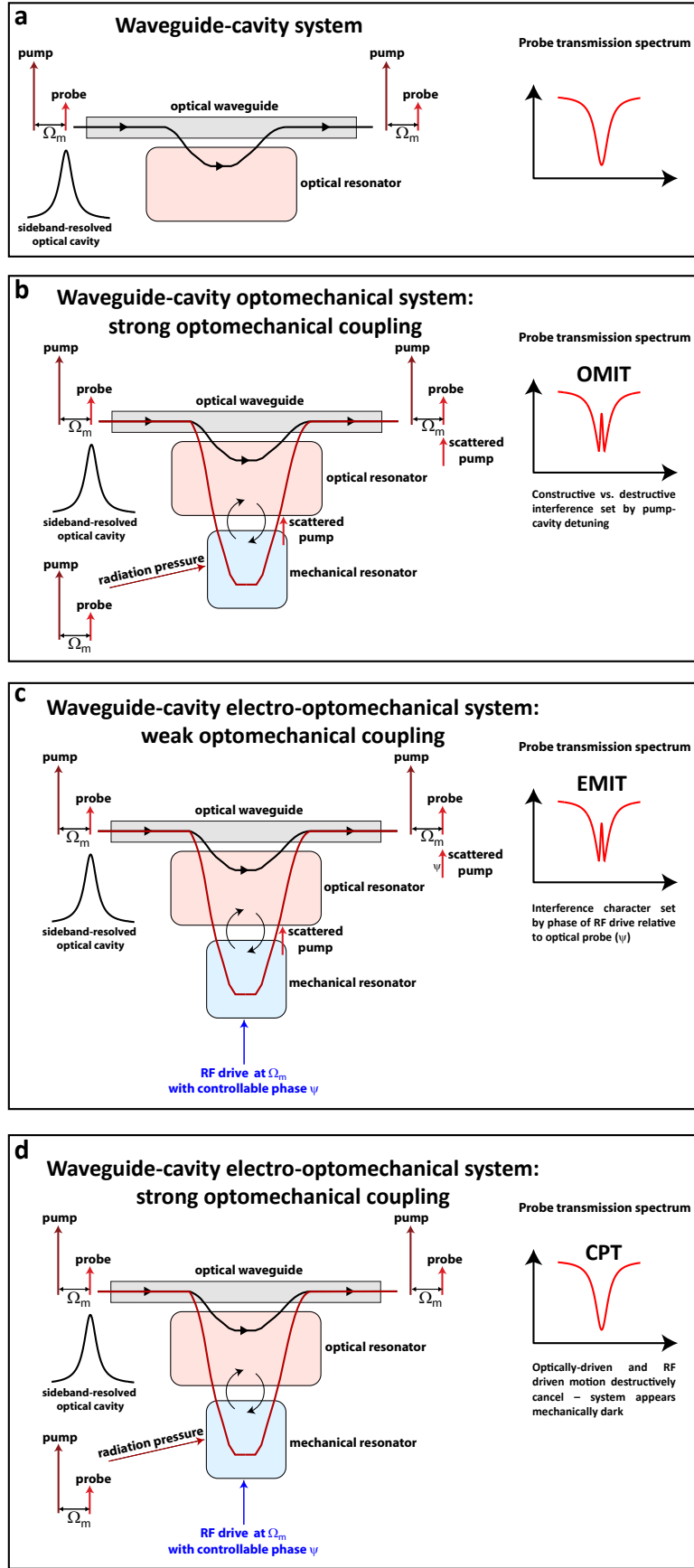
FIG. S5: Illustration of different interference effects observable in the piezo-optomechanical devices. (a) Standard optical waveguide-cavity coupling, in which the mechanical mode does not play a role (optomechanical and electromechanical coupling are set to zero); (b) optomechanically-induced transparency (OMIT); (c) electromechanically-induced optical transparency (EMIT); (d) acoustic coherent population trapping (CPT). For simplicity, the figures consider the sideband-resolved regime in which only one sideband produced by phase modulation of the optical pump interacts with the system.
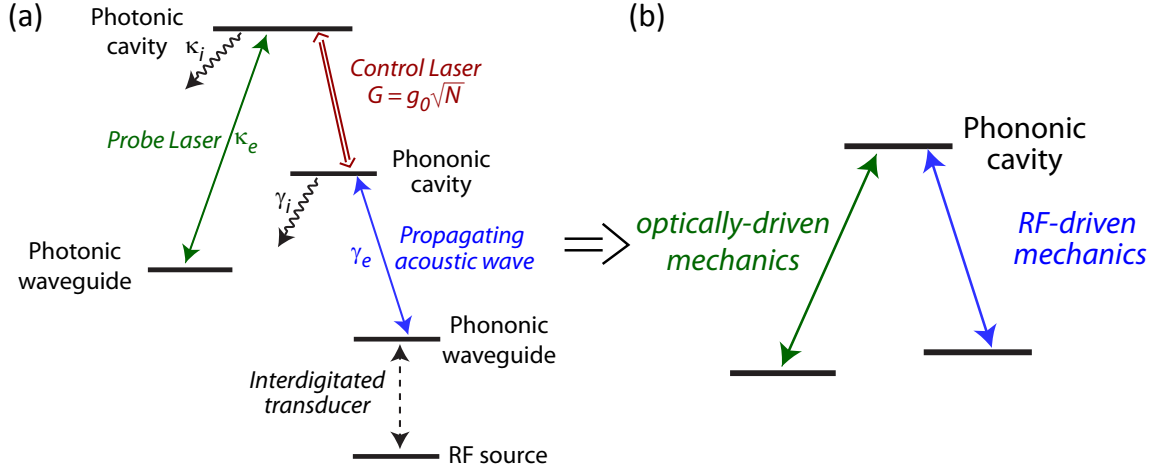
FIG. S6: (a) Schematic level diagram for the piezo-optomechanical circuit, re-displayed from Figure 4(a) of the main text. (b) Effective 3-level Λ system for phonons indicating the optomechanically-driven and RF-driven pathways.

Finally, we note that an effect analogous to OMIT, but now consisting of a transparency in the spectrum of propagating acoustic probe phonons due to coupling to intracavity photons, should also be observable in this system.

XIV. ABSENCE OF PERFECT CANCELLATION IN ACOUSTIC WAVE INTERFERENCE

The inability to achieve perfect cancellation (a flat transmission spectrum in either the cyan curve from Figure 4(c), or Figure 4(e), curve ii) can be attributed to the difference between the optomechanical (K_{om}) and electromechanical (K_{em}) transduction spectra for different mechanical modes in the optomechanical cavity. To illustrate this, we consider the difference between the OMIT response wherein we are primarily measuring the optomechanical transduction coefficient and the electro-optic S_{21} measurement wherein we measure the product of the two:

$$PSD_{OMIT} \propto K_{\mathrm{om}}(\Omega) \tag{S46}$$

$$PSD_{EO-S21} \propto K_{\mathrm{em}}(\Omega)K_{\mathrm{om}}(\Omega) \tag{S47}$$

The optomechanical transduction (K_{om}) is calculated by an overlap integral between the localized optical and mechanical modes whereas the electromechanical transduction is estimated by an overlap integral between the localized mechanical mode and the surface acoustic wave incident on the cavity. When a surface acoustic wave is incident on the cavity, it excites a superposition of all the mechanical modes of the cavity which lie within the given frequency range and the corresponding mode amplitudes are given by the corresponding transduction coefficients.

This helps us understand why the two spectra appear different (shown in Figure S7 (a)). In an OMIT measurement, the only mode that is excited with significant amplitude is a mode with strong optomechanical coupling (in this case, the localized breathing mode) and hence, the power spectral density has a Lorentzian lineshape corresponding to a single mode. When a propagating acoustic wave is incident on the cavity, other modes which might have small optomechanical coupling but significant electromechanical coupling (due to a strong overlap with the propagating acoustic wave) also appear in the measured transmission spectrum. Since the acoustic wave interference condition requires both the modes to have similar optomechanical and electromechanical transduction for the cancellation to occur, only the breathing mode is cancelled while the other excitations are not. This leads to the appearance of residual peaks and a non-flat background in the transmission spectrum. (Note: we believe these additional mechanical modes occur due to fabrication imperfections in the dimensions of the elliptical holes in the nanobeam cavity).
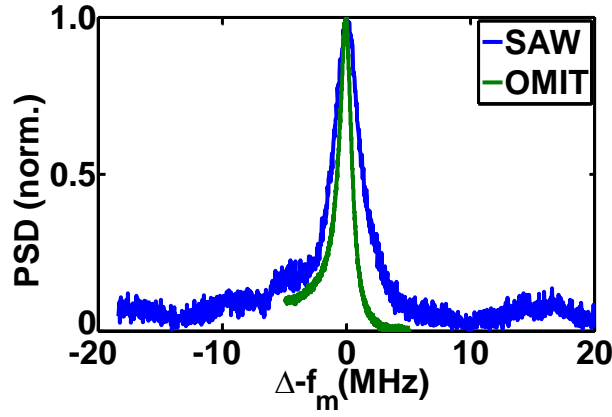
FIG. S7: (a) Normalized probe transmission for a nanobeam optomechanical cavity when the mechanical mode is coherently driven (i) optically (OMIT, green curve) and (ii) acoustically, through a surface acoustic wave excited by the IDT (SAW, blue).

XV.   ACOUSTIC WAVE INTERFERENCE FOR A NANOBEAM CAVITY WITH TWO CLOSELY SPACED MECHANICAL MODES

As illustrated in the previous section, different closely spaced mechanical modes can have vastly different optomechanical and electromechanical coupling coefficients. This enables us to demonstrate conclusively that the acoustic wave interference condition shown in Figure 4(c) in the main text occurs in the mechanical domain due to a cancellation between the optomechanical and electromechanical drive terms.

Figure S8 shows an optomechanical nanobeam cavity with two closely spaced mechanical modes, one the breathing mode which has both strong optomechanical and electromechanical coupling and a second mode which has strong electromechanical coupling but weak optomechanical coupling. We use the exact same procedure as in Figure 4(c) to probe the device. Starting with no RF power applied to the IDT, we see a single Lorentzian peak corresponding to OMIT (black curve) wherein only the mode with strong optomechanical coupling is visible. As we increase the RF power to the IDT keeping the phase set for acoustic wave interference, we see that the first mode decreases in amplitude whereas the second (higher frequency) mode rises. This opposite behaviour can be explained by noting that the first mechanical mode (breathing mode) is being driven by two terms, the optical drive term due to the beating between the carrier and the phase modulated sideband and the acoustic term due to the surface wave incident on the cavity. In contrast, the second mode is primarily driven by the propagating acoustic mode. Thus, the first mode clearly demonstrates the acoustic cancellation effect when the two driving terms are comparable in amplitude but opposite in phase whereas the second mode does not show any acoustic wave interference effect because there is only one driving term.
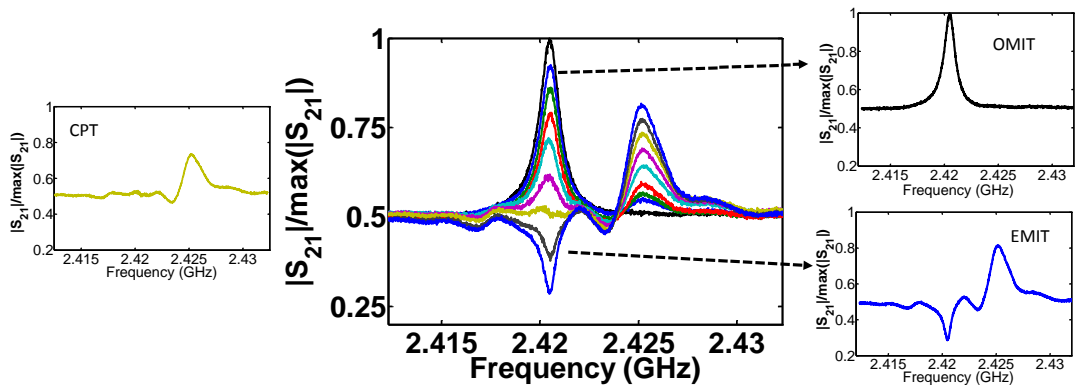

FIG. S8: Normalized probe sideband transmission amplitude as a function of increasing RF power to the IDT. The lower frequency mode (with strong optomechanical coupling) shows a clear signature of acoustic coherent population trapping whereas the higher frequency mode does not. The OMIT and EMIT cases, corresponding to zero and maximum RF power applied to the IDT, respectively, are shown separately for clarity on the right, while the acoustic coherent population trapping case (CPT) is shown separately on the left.

* Electronic address: krishna.coimbatorebalram@nist.gov

† Electronic address: kartik.srinivasan@nist.gov

1 S. Rumyantsev, M. E. Levinshten, and M. Shur, *Handbook Series on Semiconductor Parameters: Si, Ge, C (Diamond), GaAs, GaP, GaSb, InAs, InP, InSb* (World Scientific, 1999).

2 A. Khelif, B. Aoubiza, S. Mohammadi, A. Adibi, and V. Laude, "Complete band gaps in two-dimensional phononic crystal slabs," Physical Review E **74**, 046 610 (2006).

3 S. Mohammadi, A. A. Eftekhar, A. Khelif, and A. Adibi, "Simultaneous two-dimensional phononic and photonic band gaps in opto-mechanical crystal slabs," Optics Express **18**, 9164–9172 (2010).

4 Y. Pennec, B. D. Rouhani, E. El Boudouti, C. Li, Y. El Hassouani, J. Vasseur, N. Papanikolaou, S. Benchabane, V. Laude, and A. Martinez, "Simultaneous existence of phononic and photonic band gaps in periodic crystal slabs," Optics Express **18**, 14 301–14 310 (2010).

5 S. El-Jallal, M. Oudich, Y. Pennec, B. Djafari-Rouhani, A. Makhoute, Q. Rolland, S. Dupont, and J. Gazalet, "Optomechanical interactions in two-dimensional Si and GaAs phoXonic cavities," Journal of Physics: Condensed Matter **26**, 015 005 (2014).

6 M. L. Gorodetsky, A. Schliesser, G. Anetsberger, S. Deleglise, and T. J. Kippenberg, "Determination of the vacuum optomechanical coupling rate using frequency noise calibration," Optics Express **18**, 23 236–23 246 (2010).

7 K. C. Balram, M. Davanço, J. Y. Lim, J. D. Song, and K. Srinivasan, "Moving boundary and photoelastic coupling in GaAs optomechanical resonators," Optica **1**, 414–420 (2014).

8 G. Agarwal and S. Huang, "Electromagnetically induced transparency in mechanical effects of light," Physical Review A **81**, 041 803 (2010).

9 S. Weis, R. Rivière, S. Deléglise, E. Gavartin, O. Arcizet, A. Schliesser, and T. J. Kippenberg, "Optomechanically Induced Transparency," Science **330**, 1520–1523 (2010).

10 A. H. Safavi-Naeini, T. P. M. Alegre, J. Chan, M. Eichenfield, M. Winger, Q. Lin, J. T. Hill, D. E. Chang, and O. Painter, "Electromagnetically induced transparency and slow light with optomechanics," Nature (London) **472**, 69–73 (2011).

11 J. Bochmann, A. Vainsencher, D. D. Awschalom, and A. N. Cleland, "Nanomechanical coupling between microwave and optical photons," Nature Physics **9**, 712–716 (2013).

12 K. Y. Fong, L. Fan, L. Jiang, X. Han, and H. X. Tang, "Microwave-assisted coherent and nonlinear control in cavity piezo-optomechanical systems," Physical Review A **90**, 051 801 (2014).

13 E. Arimondo, *Coherent Populating Trapping in Laser Spectroscopy* (Elsevier Science, 1996), pp. 257–354.

14 S. Khan, M. Kumar, S. R. Chanu, V. Bharti, and V. Natarajan, "Coherent population trapping (CPT) versus Electromagnetically induced transparency (EIT)," arXiv:1503.06956 (2015).